bus-7 TOMS during periods when the Meteor-3 crosses the equator between 9 a.m. and 3 p.m. There have been five such periods of about 2 months each since its launch. During these periods (Fig. 5), the Nimbus-7 TOMS and Meteor-3 TOMS data show a consistent 1% bias. (In practice, the Meteor-3 TOMS data compare well with the Nimbus-7 TOMS data over a much wider range of equator crossing times.) The Meteor-3 comparison confirms that the interpolated calibration for the period February 1992 to September 1992 is accurate, and that the calibration did not shift in 1992.

The stability of TOMS is monitored relative to ozone observations made each summer at the Mauna Loa observatory with the World Standard Dobson Instrument 83 (I83) (8). The calibration of I83 has been maintained since 1962 to an accuracy of ±0.5% (9). These comparisons indicate that the TOMS ozone measurements have been stable relative to I83 to approximately 0.5% (Fig. 6). The TOMS-I83 comparison in July and August 1992 is consistent with the comparison in previous years. The I83 comparison is a good test of the aerosol sensitivity of the TOMS measurements. Dobson measurements, because they are done with a pair of wavelength pairs, are not sensitive to contamination by the presence of atmospheric aerosols. The consistency of the I83-TOMS comparison confirms our radiative transfer calculations that show that the aerosols have a small net effect on the TOMS measurement (6).

We also compared the TOMS data with a summer (June–August) average of 22 Dobson stations for which data were available through 1992 (Fig. 6). Only direct-sun Dobson observations were used, and all the data were adjusted to use the Bass and Paur ozone cross sections. Although there was a small trend in the TOMS-Dobson difference (possibly caused by increasing tropospheric ozone), there was not a significant change in 1992. The absolute offsets of 4.5% relative to I83 and of 3% relative to the 22-station average most likely result from an error in the original ground calibration of TOMS. Both the World Standard Dobson Instrument and the 22-station average confirm that the TOMS calibration in 1992 was consistent with that for earlier years and that the low observed ozone values are not a result of a shift in the instrument calibration.

In summary, the 1992 global average amount of ozone is 2 to 3% lower than the lowest values observed in earlier years. The largest 1992 decreases occurred during November and December, and were 3 to 4 standard deviations below the 12-year daily mean. The largest decreases occurred from 10°S to 20°S and 10°N to 60°N. Only in the equatorial region are the ozone values well within the envelope data from earlier years. It is significant that 1992 is the first time that ozone amounts observed by TOMS showed a simultaneous sustained decrease over a wide latitude range in both hemispheres.

The cause of the 1992 low ozone values is uncertain. Although the mechanism for ozone decrease is unknown, the understandable first guess would be that the decrease is related to the continuing presence of aerosol from the Mount Pinatubo eruption. There are three possibilities related to the presence of the aerosol: (i) direct chemical loss through increased heterogeneous processing (*10*); (ii) an aerosol-induced change in radiative heating which can directly affect ozone transport; or (iii) changes in photochemical production or loss rates caused by the temperature changes resulting from the aerosol heating. The size and timing of these potential effects of heterogeneous processing have been modeled by several groups (*11*). In general, these model simulations have not predicted the size or the timing of the observed ozone decreases for 1992 to 1993. Transport effects caused by aerosol-induced radiative heating were proposed (5) as the cause of the short-term tropical ozone loss observed immediately after the Mount Pinatubo eruption, but the mechanism responsible for the long-term ozone changes observed more than 1 year after the eruption remains unknown.

REFERENCES AND NOTES

1. R. S. Stolarski, P. Bloomfield, R. D. McPeters, J. R. Herman, *Geophys. Res. Lett.* **6**, 1015 (1991); J. R. Herman, R. McPeters, R. Stolarski, D. Larko, R. Hudson, *J. Geophys. Res.* **96**, 17279 (1991).
2. R. S. Stolarski *et al.*, *Science* **256**, 342 (1992).
3. R. S. Stolarski *et al.*, *World Meteorol. Org. Ozone Rep. 25* (1992).
4. First reported by J. C. Farman, B. G. Gardiner, and J. D. Shanklin [*Nature* **315**, 2017 (1985)] and confirmed as a regional phenomena by R. S. Stolarski *et al.* [*ibid.*, **322**, 808 (1986)].
5. S. Kinne, O. Toon, M. J. Prather, *Geophys. Res. Lett.* **19**, 1927 (1992); S. Chandra, *ibid.* **20**, 33 (1993); M. R. Schoeberl, P. K. Bhartia, E. Hilsenrath, O. Torres, *ibid.*, p. 29.
6. J. R. Herman *et al.*, *J. Geophys. Res.* **96**, 7531 (1991).
7. P. K. Bhartia, J. R. Herman, R. D. McPeters, O. Torres, in preparation.
8. R. D. McPeters and W. D. Komhyr, *J. Geophys. Res.* **96**, 2987 (1991).
9. W. D. Komhyr *et al*, *ibid.* **94**, 9847 (1989).
10. D. J. Hofmann and S. Solomon, *ibid.*, p. 5029.
11. M. J. Prather, *ibid.* **97**, 10187 (1992); G. Brasseur and C. Granier, *Science* **257**, 1239 (1992); C. Granier and G. Brasseur, *J. Geophys. Res.* **97**, 18015 (1992).

12. We thank J. Kerr for providing the Dobson data from the World Ozone Data Centre, Atmospheric Environment Service, Downsview, Ontario. The support of J. H. Lienesch and H. D. Bowman and the NOAA Climate and Global Change Program in developing the SBUV/2 data set is gratefully acknowledged.

11 March 1993; accepted 30 March 1993

Tectonics and Volcanism of Eastern Aphrodite Terra, Venus: No Subduction, No Spreading

Vicki L. Hansen* and Roger J. Phillips

Eastern Aphrodite Terra, a deformed region with high topographic relief on Venus, has been interpreted as analogous to a terrestrial extensional or convergent plate boundary. However, analysis of geological and structural relations indicates that the tectonics of eastern Aphrodite Terra is dominated by blistering of the crust by magma diapirs. The findings imply that, within this region, vertical tectonism dominates over horizontal tectonism and, consequently, that this region is neither a divergent nor a convergent plate boundary.

Eastern Aphrodite Terra, the region on Venus between Alta and Thetis regiones, is approximately equal in size to the western North American cordillera, between Mexico and Alaska. This region on Venus is part of the Equatorial Highlands, which is characterized by large topographic relief and free-air gravity anomalies, intense tectonism, and volcanism (*1–3*). Its size and landforms make it an area important to the study of the tectonics of Venus. Using Pioneer Venus data, Schaber (4) suggested that this region recorded limited global extension, but others (5) proposed that it represents a zone of crustal divergence, analogous to terrestrial mid-ocean ridges. Data from the National Aeronautics and Space Administration–sponsored Magellan project have broadened the interpretation of this region. Eastern Aphrodite Terra has been interpreted as part of a circumglobal rift zone separating two major venusian

V. L. Hansen, Department of Geological Sciences, Southern Methodist University, Dallas, TX 75275.
R. J. Phillips, McDonnell Center for the Space Sciences and Department of Earth and Planetary Sciences, Washington University, St. Louis, MO 63130.

*To whom correspondence should be addressed.

plates (6), on the basis of SAR (synthetic aperture radar) data, and as a region of convergence and subduction (7), from altimetry data. McKenzie and colleagues (7) argued that some Venus trenches display the same curvature and topographic asymmetry as terrestrial subduction zones. Sandwell and Schubert (8, 9) contended that some corona trenches (10) and outboard topographic highs are consistent with a model of lithospheric subduction in which lithosphere exterior to the corona is subducting inward, overthrust by the spreading corona. High-resolution Magellan SAR images of the venusian surface and altimetry data provide a means to study crustal deformation of this area. We examined the geology and structures of a portion of eastern Aphrodite Terra displayed in the Magellan SAR CMIDR (compressed mosaicked image data record; 225 m per pixel) 15S, 163 (Fig. 1). In this report, we present geological and structural relations that indicate that eastern Aphrodite Terra is analogous to neither a divergent nor a convergent plate boundary but is best explained by a model of deformation and volcanism that result from blistering of the crust by magma diapirs.

Eastern Aphrodite Terra comprises a band of circular structures and east-trending fractures that extend from the Artemis corona–Thetis Regio region east to Atla Regio (Fig. 1). The belt is 1500 km wide and >8000 km long. The circular structures vary in diameter from 100 to 2600 km and fit the descriptions of coronas or novae (10–12). Most display radial or concentric fractures, or both, that typically extend along 180° to 270° of their perimeter, although 360° ring fractures are preserved locally, particularly for rings of small diameter. Some circular structures may have as many as four nested sets of concentric fractures, each separated by a region that is marked by little or no deformation. Fractures from one structure commonly overlap those of adjacent structures. These structures are commonly sites of extensive volcanism.

We mapped individual framelets (56 total) of CMIDR 15S, 163 to construct a composite map. This region contains three circular structures [centers at 14S, 164E (Miralaidji); 17S, 162E; and 15.5S, 158.5E] that lie between Diana and Dali chasmata, which are topographic troughs with steep ridges to the south and north, respectively. A north-trending, eastward concave fold belt that may form the western boundary of circular structure 17S, 162E lies between Diana and Dali chasmata. Latona corona, an eye-shaped structure in the southeast part of the CMIDR, comprises several overlapping circular structures. The bright areas of the structures are ridges, and parallel dark areas are troughs. Part of a similar eye-shaped structure appears in the northwest corner of the map area.

In the subduction model (7), Diana and Dali chasmata represent south- and north-dipping subduction zones, respectively, and the fold belt west of 17S, 162E represents a right-lateral transform fault. The ridge and trough pairs that mark the eye shape of Latona and the similar structure in the northwest are also defined as oppositely verging subduction zones with the eye-shaped crustal blocks as the upper plate. Although the rift-zone model is not described in detail, each of the troughs interpreted as a subduction zone (7) appears to be interpreted as a rift zone (6).

Three key areas provide evidence for the tectonic evolution of this part of eastern Aphrodite Terra: Miralaidji, the southwest boundary of Latona, and the region north of Diana chasma (Fig. 1). Miralaidji is defined as a radial-concentric corona (11) and is described by Squyres and colleagues (12). This area is ~650 km in diameter and, as the classification indicates, is composed of spectacular radial fractures ringed by two obvious sets of concentric fractures at 190 and 250 km in the southeast quadrants of the northwest trough (Figs. 1 and 2). A set of inner concentric fractures is poorly preserved along an arc of ~110° south of 14S, 164E. The radial fractures cut the inner concentric fractures but are themselves cut by east-striking fractures that cut across, and obscure, the inner concentric fracture set (13). In contrast, the outer concentric fractures commonly truncate and offset radial fractures in a dip-slip manner. Thus, radial and concentric fracture sets are not everywhere temporally equivalent.

Extensive lava flows emanate from both radial and concentric fractures. Radar-dark flows fill many radial fractures (for example, 15.5S, 158.5E; Fig. 1) as well as a moat outside the outer concentric fracture set of Miralaidji (Fig. 2). The boundaries of these

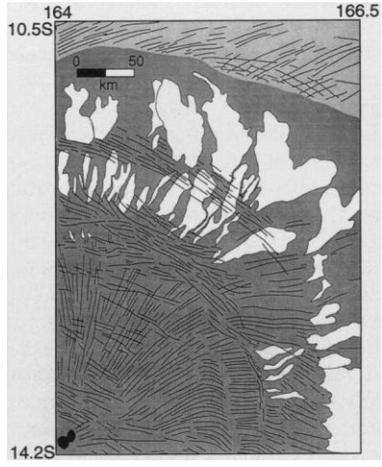

Fig. 2. Geologic map of the northeast portion of Miralaidji corona. Radar-dark flows are in dark gray; radar-bright flows are in white.

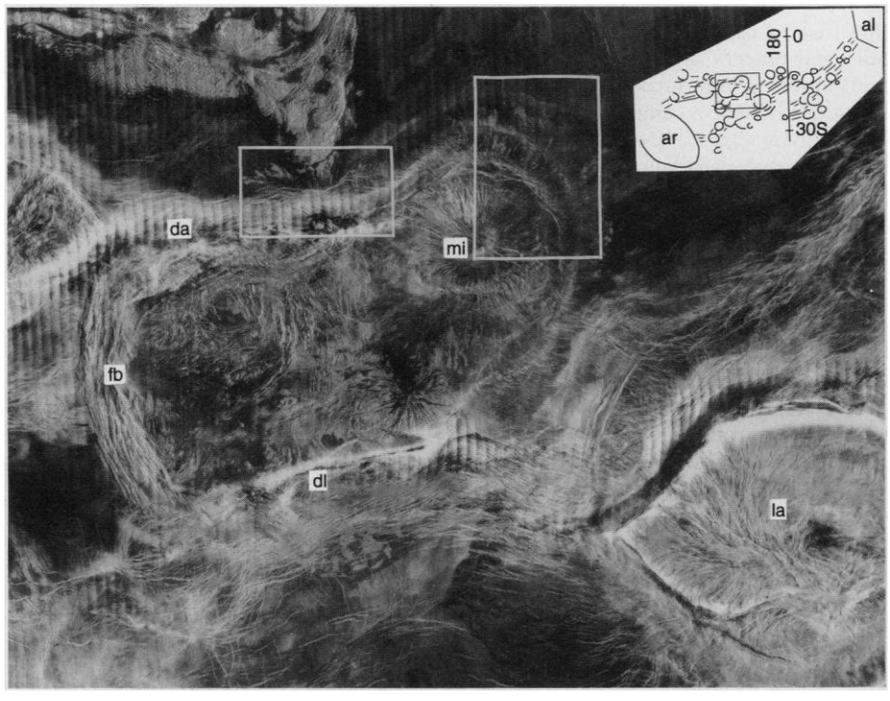

Fig. 1. Magellan SAR image of CMIDR 15S, 163, eastern Aphrodite Terra. Abbreviations: da = Diana chasma; dl = Dali chasma; fb = fold belt; mi = Miralaidji corona; la = Latona corona. The southwest corner is 22.6S, 153.7E; the northeast corner is 8.5S, 171.9E; and the image is ~1850 km across. Boxes show locations of Figs. 2 and 5. Inset sketch map shows circular features and regional fractures of eastern Aphrodite Terra from Alta Regio (al) to Artemis (ar), simplified from a sinusoidal projection ~14N, 180E. The location of 15S, 163 is shown by the box.

flows are influenced by local topography, whereas radar-bright flows form lobate structures and define their own boundaries. Therefore, we interpret radar-dark flows as generally less viscous than radar-bright flows. The origin of radar-dark flows is uncertain because they flood broad regions. In the southern part of Miralaidji, radar-bright flows originate from a region apparently swamped by radar-dark flows that fill radial fractures (Fig. 1). In the northeast, radar-bright flows emanate from the prominent concentric fractures. Fractures in the outer set cut flows that originate from the inner fracture set; hence, the concentric fractures, and associated volcanism, are interpreted to young outward.

Latona, like Miralaidji, displays several generations of fractures that form concentric or radial to bow tie–shaped patterns (Fig. 3). Local radar-dark regions among these fractures are interpreted as lava flows. Concentric fractures are found along the leading edge of the topographic high and the steep inner slope of the troughs that define the boundary of Latona. The radial fractures, filled locally by lava, make up a tightly spaced, penetrative fabric that can be traced across the region of less penetrative, more widely spaced concentric fractures (Fig. 4). The orientation and number of radial fractures do not change outwardly (Fig. 3). Radial fractures are interpreted as relatively shallow features that are offset in a dip-slip way by deeper concentric fractures that act as normal faults. Because the radial and concentric fractures share a common center, as in Miralaidji, these fracture sets probably have a common origin.

Prominent regional lineaments that trend east to east-northeast and parallel eastern Aphrodite Terra (Fig. 1) postdate formation of most of the circular structures, such as Miralaidji (*12*) and Latona. The character of the lineaments is difficult to distinguish because of their shallow angle relative to the radar path direction. We interpret them as fractures because they have sharp boundaries and are relatively straight and continuous (that is, they do not anastomose). The nature of the lineaments may change along strike, although they do not deform the circular shape of the structures and so are not responsible for significant crustal strain. They are similar to regional extensional fractures of the Guor Linea trough region of Eistla Regio (*14*) and accommodate only minor crustal displacement.

The two outer concentric fracture sets of Miralaidji become parallel with Diana chasma, which parallels the regional east-trending fractures. Radar-dark volcanic flows mark the axis of Diana chasma and flood the region to the north. Radar-bright flows emanated and flowed north from east-trending fractures north of Diana chasma (Figs. 1 and 5) that are located on the outboard side of the topographic bulge that is interpreted as a flexed subducting plate (*7*, *9*). Radar-bright flows in a similar structural position are also seen south of Dali chasma. The north-trending ridge belt that joins Diana and Dali chasmata (Fig. 1), interpreted as a right-lateral fault zone in the subduction model (*7*), comprises asymmetric and anastomosing ridges that indicate it is a fold belt (*15*). Because we found no evidence of strike-slip offset along or within this belt, we concur (*15*) that it shows dominantly east-west coaxial shortening.

These magmatic and structural relations from eastern Aphrodite Terra are consistent with a model in which magma diapirs have blistered the crust in a zone of regional lithospheric tension [for example, (*16*, *17*)]. In our model a magma diapir rises to the base of the crust and spreads laterally. The buoyant magma lifts up the crust, causing radial and concentric fracturing (*11*, *12*, *18*). If the fractures are deep enough to allow the ascent of magma to the surface, volcanism results. Because the smallest circular structures are generally free of volcanism, their fractures evidently did not extend deep enough to tap melt. Radial fractures propagate outward during crustal uplift, and concentric fractures form along the outer edge of the crustal blister during periods of crustal relaxation (*18*). As the crust cools and the uplift relaxes, the blisters take on the topography characteristic of coronas that have a broad, central low surrounded by a ringed topographic ridge and an outboard moat (*11*, *12*, *18*). Although the brittle crust is thinned and extended above the diapir, the crust as a whole is thickened by magmatism.

As the magma differentiates at depth, less dense and perhaps more silica-rich magma concentrates at the top of the magma chamber or in regions of greatest local tensile stress. Less differentiated and less viscous radar-dark flows commonly predate the more viscous radar-bright flows. Magma that leaks from the concentric fractures flows outward into the moat. As more magma is added at depth, the blister expands and a new combination of outer ridge, concentric fracture set, and moat forms and crosscuts earlier lava flows. This process continues until magma ceases to rejuvenate the subsurface magma pool. The development of any blister probably reflects

Fig. 3. Lineament map of western Latona corona. The gray lines mark the approximate axes of the northern and southern troughs, which are interpreted as south- and north-dipping subduction zones, respectively (*7*). The box shows the region illustrated in Fig. 4.

Fig. 4. Magellan SAR image of a part of the southwest boundary of Latona corona (Fig. 3), including the topographic trough, proposed as a subduction zone (*7*). Note the trace of delicate radial fractures across the trough. The horizontal scale is ~200 km.

Fig. 5. Geologic map of the region north of and including Diana chasma. Radar-dark lava flows (black) mark the axis of the trough; radar-bright lava flows (white) overprint radar-dark flows (dark gray) that flood regions in and around tessera (patterned). A ridge ~3 km high parallels the trough just south of the map area; a low ridge, which also parallels the trough, lies between the black lava flows and the radar-bright flows to the north.

local crustal structure among other factors.

We propose that magma diapirs formed similar coronae throughout eastern Aphrodite Terra. Our model is similar to that proposed for corona evolution (*11, 12, 18*). However, Stofan and colleagues (*11*) proposed that coronas, such as those in eastern Aphrodite Terra, and large hot spots such as Beta Regio all originated as thermal plumes on the core-mantle boundary. In contrast, we believe that coronas form from magmas derived from the upper mantle, probably as buoyantly unstable partial melt (*16*) that forms ponds at the base of the crust. Our model includes a hot (relative to Earth at the same pressure) Venus mantle that supplies significant magma at sublithospheric depths. Our findings indicate that volcanism occurs throughout the evolution of coronas and apparently changes their composition over time. The evidence that episodes of volcanism overlapped with concentric fracture formation shows that diapir spreading and gravitational relaxation are closely related in time (*12, 18*). A compositional rather than a thermal source for the rising diapir provides a means to explain the intimate relation between volcanism and tectonism observed at coronas, although thermal plumes that undergo pressure-release partial melting in the upper mantle cannot be ruled out. However, the considerable range of corona sizes [60 to 2600 km (*11*)] suggests that, if they have a common origin, it is in the upper mantle, and mechanisms beyond thermal boundary layer instability are required. We propose that the availability of magma determines the ultimate size of any corona.

Dominantly east-trending fractures that formed after and obscure the formation of coronae most likely reflect late, perhaps ongoing, lithospheric tension in eastern Aphrodite Terra. Further, the correlation between extensional environments and coronas is consistent with the melt instability model: Horizontal stretching of the lithosphere leads to the time-dependent vertical strain required to initiate the instability. The interaction between regional and concentric fractures is generally responsible for the present regional topography of eastern Aphrodite Terra. Diana and Dali chasmata result from spatial overlap of concentric fractures from at least three adjacent circular structures (14S, 164E; 17S, 162E; and 15.5S, 158.5E) and east-trending regional fractures. The eye-shaped structure of Latona results from the intersection of concentric fractures of overlapping circular structures.

The structures of eastern Aphrodite Terra are not akin to the large-scale structures of either spreading rift zones (*3*) or terrestrial convergent margins. Rifting of terrestrial crust results in a linear array of structures about a central trough that may be offset by transform faults or transfer zones. Circular structures on the scale of eastern Aphrodite Terra are not evident. One might compare eastern Aphrodite Terra to intracontinental rift systems such as the Rio Grande or East African rifts. The large difference in width (more than ten times) and the absence of a central rift valley in eastern Aphrodite Terra make direct analogy with the East African rift inappropriate. Like the Rio Grande rift, eastern Aphrodite Terra may represent a broad region of diffuse crustal extension, but it is not a fundamental plate boundary. With regard to the subduction analog, there is widespread evidence for volcanism in both the upper and lower plates of the proposed subduction regime, which is unlike the case on Earth. A subduction interpretation must account for the volcanism that accompanies syn-subduction structures within the proposed upper plate, trench, and lower plate.

If, as postulated (*7–9*), the troughs in this region are formed where the lower plate is recycled into the mantle, then the structural history of the upper and lower plates should differ, as it does on Earth. However, radial fractures extend across a proposed trench, as in the case of Latona (Figs. 3 and 4), without any appreciable offset. If radial fractures formed across a postulated plate boundary before subduction, then there should be a mismatch in fracture orientation and density across the trench (*19*). Individual radial fractures can be traced across the trough (Fig. 4), and a mismatch of neither fracture orientation nor density has been observed (Fig. 3). Furthermore, most of the radial fractures are the oldest fractures associated with coronas (*12*). Therefore, concentric fractures postdate radial fractures but also coincide with the topographic high; this high could be interpreted as having formed contemporaneously with a subduction trench. Clearly, the observed temporal evolution is not consistent with the subduction model. In addition, formation of radial fractures after subduction would require that the penetrative radial fabric was not affected by the lithosphere-scale plate boundary (*13*).

An alternative explanation for the trough and inboard topographic high is that they form during gravitational relaxation of an isostatically uncompensated plateau (*18*). However, this proposal also has problems: (i) It is difficult to imagine that coronas would remain uncompensated well into their evolution; (ii) the relatively narrow widths of the trough and inboard high require that the sides of the plateau are nearly vertical when relaxation starts; and (iii) the relaxation process does not seem to account for the outboard topographic high (*18*). If, as in our model, a magma blister forms coronas, additional factors could affect evolution and relaxation, such as lateral variations in lithospheric strength, mechanical uncoupling at the base of the crust, and flexural loading by intruded material.

One implication of our model is that, at one time, magma lay not far below the surface along the entire length of eastern Aphrodite Terra. It also suggests that magma diapirs arise in response to large-scale regional strain, but access to the surface is aided by tension associated with the formation and evolution of individual coronae. The near ubiquitous occurrence of relatively shallow magma sources has been proposed independently on the basis of the widespread occurrence of radar-dark floors in all but the youngest impact craters (*20*). Finally, this model implies that, although the crust may be locally thickened and extended, the amount of crustal extension is minor (<5 to 10%) across the width of the belt. Crustal thickening results mostly from the addition of magmatic material rather than from crustal duplication that results from underthrusting or subduction.

REFERENCES AND NOTES

1. R. J. Phillips and M. C. Malin, in *Venus*, D. M. Hunten *et al.*, Eds. (Univ. of Arizona Press, Tucson, 1983), p. 159.
2. _____, *Annu. Rev. Earth Planet. Sci.* **12**, 411 (1984).
3. S. C. Solomon *et al.*, *J. Geophys. Res.* **97**, 13199 (1992).
4. G. G. Schaber, *Geophys. Res. Lett.* **9**, 499 (1982).
5. J. W. Head III and L. S. Crumpler, *Science* **238**, 1380 (1987).
6. J. Suppe and C. Connors, *Lunar Planet. Sci.* **23**, 1389 (1992).
7. D. McKenzie *et al.*, *J. Geophys. Res.* **97**, 13533 (1992).
8. D. T. Sandwell and G. Schubert, *ibid.*, p. 16069.
9. _____, *Science* **257**, 766 (1992).
10. Geological structures on Venus characterized by an annulus of concentric tectonic features; E. R. Stofan and J. W. Head, *Icarus* **83**, 216 (1990).
11. E. R. Stofan *et al.*, *J. Geophys. Res.* **97**, 13347 (1992).
12. S. W. Squyres *et al.*, *ibid.*, p. 13611.
13. It is generally inferred in fracture studies that truncated fractures must be younger because the older fracture acts as a free surface blocking propagation of the younger fracture. However, if the older fracture is filled, it does not act as a free surface, or if the younger fracture is initiated at a greater depth than that of the older fracture, the younger fracture can cut it. The depth of a fracture set is related to the spacing of the fractures. The more closely spaced, or penetrative, the fractures, the more shallow is their depth.
14. R. E. Grimm and R. J. Phillips, *J. Geophys. Res.* **97**, 16035 (1992).
15. F. Bilotti, C. Connors, J. Suppe, *Lunar Planet. Inf. Contrib.* **789**, 10 (1992).
16. P. J. Tackley and D. J. Stevenson, *Eos* **72**, 287 (1991).
17. R. R. Herrick and R. J. Phillips, *J. Geophys. Res.* **97**, 16017 (1992).
18. D. M. Janes, *et al.*, *ibid.*, p. 16055.
19. If a subduction zone is at radius $R1$ and material at radius $R2$ is brought into the trench, then the jump in radial fracture density across the trench should be $R2/R1$ (if the radial fractures are orthogonal to the concentric trench—a reasonable assumption). We concentrated on the western part of the northernmost of the three southern pro-

posed trenches of Latona. In formulating their model, Sandwell and Schubert (*8, 9*) analyzed the topography of the eastern part of the southernmost trench. The full-resolution, mosaicked image data record for this region (FMIDR 25S, 174 at 75 m per pixel) shows that concentric fractures extend from the proposed inner topographic high across the trench to the outer high and seem related to the formation of all three proposed trenches. Radial fractures are poorly developed here, and their temporal relation to the concentric fractures is unclear. However, a few radial fractures can be traced across the proposed plate boundary, and overall there is no change in fracture density across this boundary.

20. R. J. Phillips *et al.*, *J. Geophys. Res.* **97**, 15923 (1992).

21. Supported by the National Aeronautics and Space Administration Planetary Geology and Geophysics Program under grant NAGW-2915 to Southern Methodist University and grant NAGW-3024 to Washington University. We thank J. W. Goodge, G. E. McGill, and an anonymous reviewer for their comments and suggestions.

1 December 1992; accepted 18 February 1993

Molecular Basis for Specific Recognition of Both RNA and DNA by a Zinc Finger Protein

Karen R. Clemens, Veronica Wolf, Steven J. McBryant, Penghua Zhang, Xiubei Liao, Peter E. Wright,* Joel M. Gottesfeld*

Transcription factor IIIA (TFIIIA) from *Xenopus* oocytes binds both the internal control region of the 5*S* ribosomal RNA genes and the 5*S* RNA transcript itself. The nucleic acid binding domain of TFIIIA contains nine tandemly repeated zinc finger motifs. A series of precisely truncated forms of this protein have been constructed and assayed for 5*S* RNA and DNA binding. Different sets of zinc fingers were found to be responsible for high affinity interactions with RNA and with DNA. These results explain how a single protein can exhibit equal affinities for these two very different nucleic acids.

Developing *Xenopus* oocytes accumulate massive quantities of ribosomal RNAs (rRNAs). Transcription factor IIIA (TFIIIA) serves both as a positive transcription factor for the synthesis of 5S RNA (*1*) and as a storage protein for 5S RNA prior to the assembly of ribosomes during the late stages of oogenesis (*2*). Since the discovery of the zinc finger nucleic acid–binding motif in TFIIIA (*3*), the mode of interaction of this protein with both DNA and RNA has been the subject of intensive investigation. TFIIIA contains a tandem arrangement of nine zinc finger motifs; each motif contains approximately 30 amino acids (*3, 4*) (Fig. 1) with invariant cysteine and histidine residues that coordinate a single zinc atom (*5*). A COOH-terminal 10-kD domain is required for the transcriptional activity of the protein (*6*); however, this domain does not interact directly with either 5S RNA (*7*) or DNA (*6, 8*) but rather is responsible for protein-protein interactions with other components of the transcription complex (*8*).

The DNA binding site for TFIIIA is contained within the 5S RNA coding sequence and consists of three short promoter elements: A 5′ A-block, an intermediate element, and a 3′ C-block (*9*). With the use of a series of recombinant fragments of TFIIIA, we have shown that the first three NH_2-terminal zinc fingers bind with full specificity to the 3′ C-block promoter element of the gene and contribute 95% of the binding energy for DNA (*10*). This interaction occurs through base-specific major groove and phosphate contacts (*10, 11*). Finger 5 binds in the major groove of the intermediate promoter element and fingers 7 to 9 bind in the major groove of the promoter A-block. Fingers 4 and 6 each bind across the minor groove, spanning these promoter elements (*10, 12*). In contrast to our knowledge of the mode of interaction of TFIIIA with DNA, relatively little is known about the mechanisms of interaction of TFIIIA with 5S RNA. RNA footprinting and chemical-crosslinking experiments (*13*) have been performed to map the binding site for TFIIIA on 5S rRNA and the results of these experiments show that TFIIIA interacts with a large portion of the 5S RNA molecule. In addition, site-specific mutagenesis studies have shown that base changes that disrupt the secondary structure of 5S RNA impair TFIIIA binding (*14*). However, the location of specific zinc fingers on 5S RNA is unknown. Because TFIIIA exhibits comparable affinities for both the 5S gene promoter and 5S rRNA (dissociation constant $K_d \cong 1$ nM) (*7, 14*), this raises the question of whether the same or different zinc fingers are utilized for high affinity binding to DNA and 5S rRNA.

To identify the zinc fingers of TFIIIA that are responsible for binding 5S rRNA we have generated two series of polypeptides that contain precise deletions of zinc fingers from either the COOH-terminus or both termini of the protein (Fig. 1). Zinc finger deletions were generated from the full-length cDNA for TFIIIA (*4*) by polymerase chain reaction (PCR) cassette mutagenesis with the use of a series of specific oligonucleotide primers (*10, 15*). The PCR products were cloned into the expression vector pRK172 (*15*) and the truncated polypeptides were purified from *Escherichia coli* cell lysates by heparin-Sepharose ion-exchange chromatography (*10*). The amino acid sequence of these polypeptides was deduced from the coding sequence in the expression plasmids. A composite sequence, indicating the start and stop amino acids of each of the polypeptides, is shown (Fig. 1). Each of these polypeptides was tested for 5S RNA binding activity with radiolabeled RNA synthesized in vitro with T7 RNA polymerase and a synthetic 5S RNA gene template (*16*). Binding was assayed by gel electrophoresis on nondenaturing polyacrylamide gels (*10*) with increasing amounts of each of the polypeptides in separate reactions. Figure 2 provides examples of binding experiments which show the contrast between high affinity and low affinity binding. Figures 3A and 3B provide a graphical representation of the data for the complete set of zinc finger polypeptides. Dissociation constants determined from the protein titrations are given (Table 1).

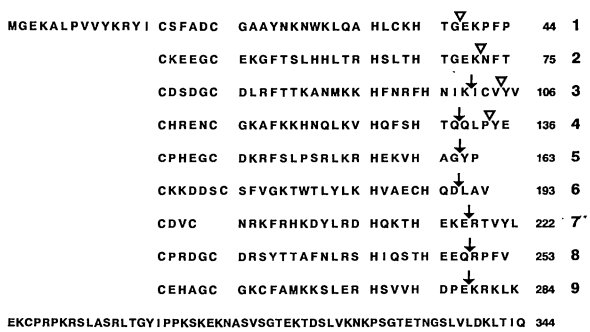

Fig. 1. Amino acid sequence of TFIIIA (*4*) with start (denoted with open triangles) and stop (denoted with arrows) positions of each of the truncated polypeptides. The start of each polypeptide was either the natural NH_2-terminus for the COOH-terminal deletions (zf1-N, where N = 3 through 9) or a Met before the indicated start amino acid for the NH_2-terminal deletions (zfN-7, where N = 2 through 5). The COOH-terminal amino acid for the latter series was Glu^{217}. The gaps within the sequence indicate regions of the zinc fingers, the loop between zinc coordinating cysteines, the finger region, the histidine loop, and the linkers between fingers.

Department of Molecular Biology, The Scripps Research Institute, La Jolla, CA 92037.

*To whom correspondence should be addressed.